NASA CR-132254

NEUTRAL BEAM DOSE AND SPUTTERING CHARACTERISTICS IN AN ION IMPLANTATION SYSTEM

A TECHNICAL REPORT

By

A.S. Roberts, Jr.

R.L. Ash

and

M.H. Berger

Prepared for the
NATIONAL AERONAUTICS AND SPACE ADMINISTRATION
Langley Research Center
Hampton, Virginia 23365

Under
Master Contract Agreement No. NAS1-9434
Task Order No. 43

School of Engineering
Old Dominion University
Technical Report 73-T1

Submitted by the
Old Dominion University Research Foundation
P.O. Box 6173
Norfolk, Virginia 23508

February 1973

Page Intentionally Left Blank

CONTENTS

FIGURES

NEUTRAL BEAM DOSE AND SPUTTERING CHARACTERISTICS IN AN ION IMPLANTATION SYSTEM

By
A.S. Roberts, Jr.[1], R.L. Ash[2] and
M.H. Berger[3]

1. INTRODUCTION

Accurate determination of ion beam dose is important in the production of ion implanted semiconductor devices. A small but significant percentage of neutral atoms in the source beam can lead to inaccuracies in impurity doping and localized sputtering of the semiconductor target in a high-vacuum ion implantation system. The work reported here discloses a technique and instrument design for calorimetric detection of the neutral atom content of a 60 keV argon ion beam. A beam sampling method is used to measure local heat flux to a small platinum wire at steady state; integration of power density profiles leads to a determination of equivalent neutral beam current. The fast neutral production occurs as a result of charge transfer processes in the region of the beam system between analyzing magnet and beam stop where the pressure remains less than 10^{-5} torr. A description of the neutral beam detector is given in section 2 along with a presentation of results.

As a part of this work, performed for the Instruments Techniques Section, Measurements Physics Branch of the Instrument Research Division, an elementary analysis of sputter material transport from target to substrate was performed; the analysis relates to semiconductor sputtering. This work with a cursory review of semiconductor sputtering literature is described in section 3. All experiments were performed using a high vacuum ion implantation system in the Instruments Techniques Section laboratories at NASA Langley Research Center.

---

1 Assistant Dean of Engineering, School of Engineering, Old Dominion University, Norfolk, Virginia 23508.
2 Associate Professor of Engineering, School of Engineering, Old Dominion University, Norfolk, Virginia 23508.
3 Graduate Student, Mechanical Engineering, Old Dominion University, Norfolk, Virginia 23508.

2. DESIGN OF NEUTRAL BEAM DETECTOR

A conventional plasma source was used to generate ionized argon; the cathode was tungsten. Extracted ions were formed into a beam via an electrostatic lens system and the beam was magnetically analyzed to produce a singly ionized argon beam in the target region. A target chamber schematic is shown in Figure 1. The target chamber is offset upward so that when the ion beam is electrostatically deflected upward and focused onto the center of the beam stop the neutral beam will continue off-center to the end of the target chamber. As indicated, the beam detector is moved up through the neutral beam. Figure 2 is a photograph of the target region assembly. The target chamber is left of center with the beam detector inserting from the bottom; below the large central tee a noble gas sputter ion pump is mounted; the beam enters from the right through the metal bellows; the vertical offset is visible by observing the bellows position. Finally, beam detection instrumentation is seen in the foreground.

2.1 Description of the Wire Detector

The problem was to devise an instrument to detect an equivalent neutral beam current down to $\sim$ .1 μa. The neutral beam is formed between the analyzing magnet and the vertical deflection plates (a distance of $\sim$ 75 cm); beam energy is assumed uniform at the value set for the ion beam, 60 keV.

A number of techniques have been employed to detect neutrals, commonly involving deposition of energy or momentum impulse (Huddlestone and Leonard, chap. 12)[1]. On the other hand, Berkner, *et al.* used a pyroelectric ceramic detector to determine neutral beam fluxes; however, the method yielded no beam structure and required simultaneously a measurement of ion beam current. A note by Ormrod disclosed an energy deposition technique where an ion beam was scanned with a tungsten wire and the resulting black-body radiation was measured. Although the method gave beam structure information it is only useful for high beam currents (significant heating of wire).

An energy deposition technique was ultimately used. A 1 mil diameter (.0254 mm) platinum wire, $\sim$ 2 cm in length, was swept through the beam, subtending the beam in a chord-wise fashion. Since beam diameters were 7 to 10 mm

[1]See Reference list.

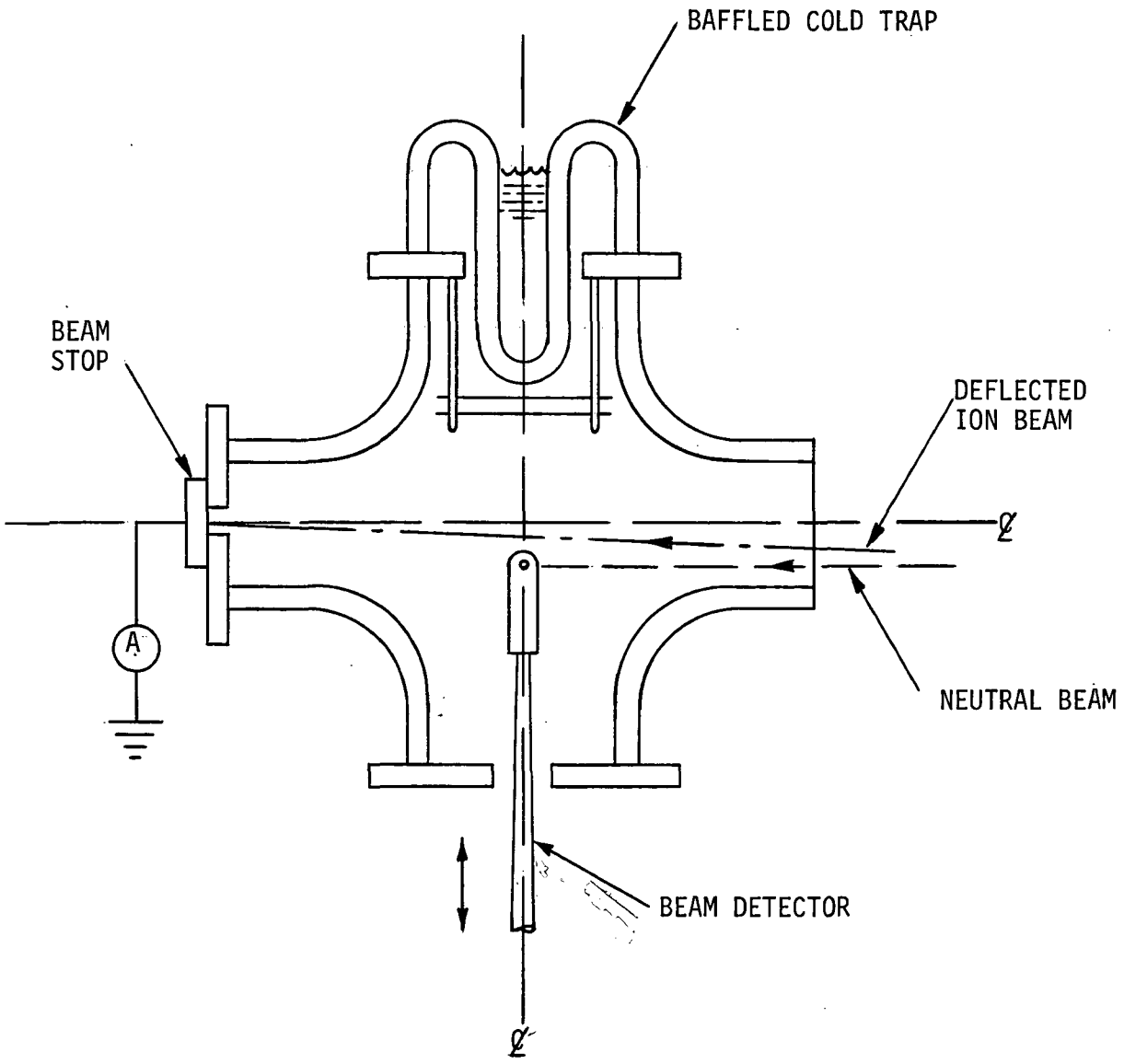

Figure 1. Target chamber schematic.

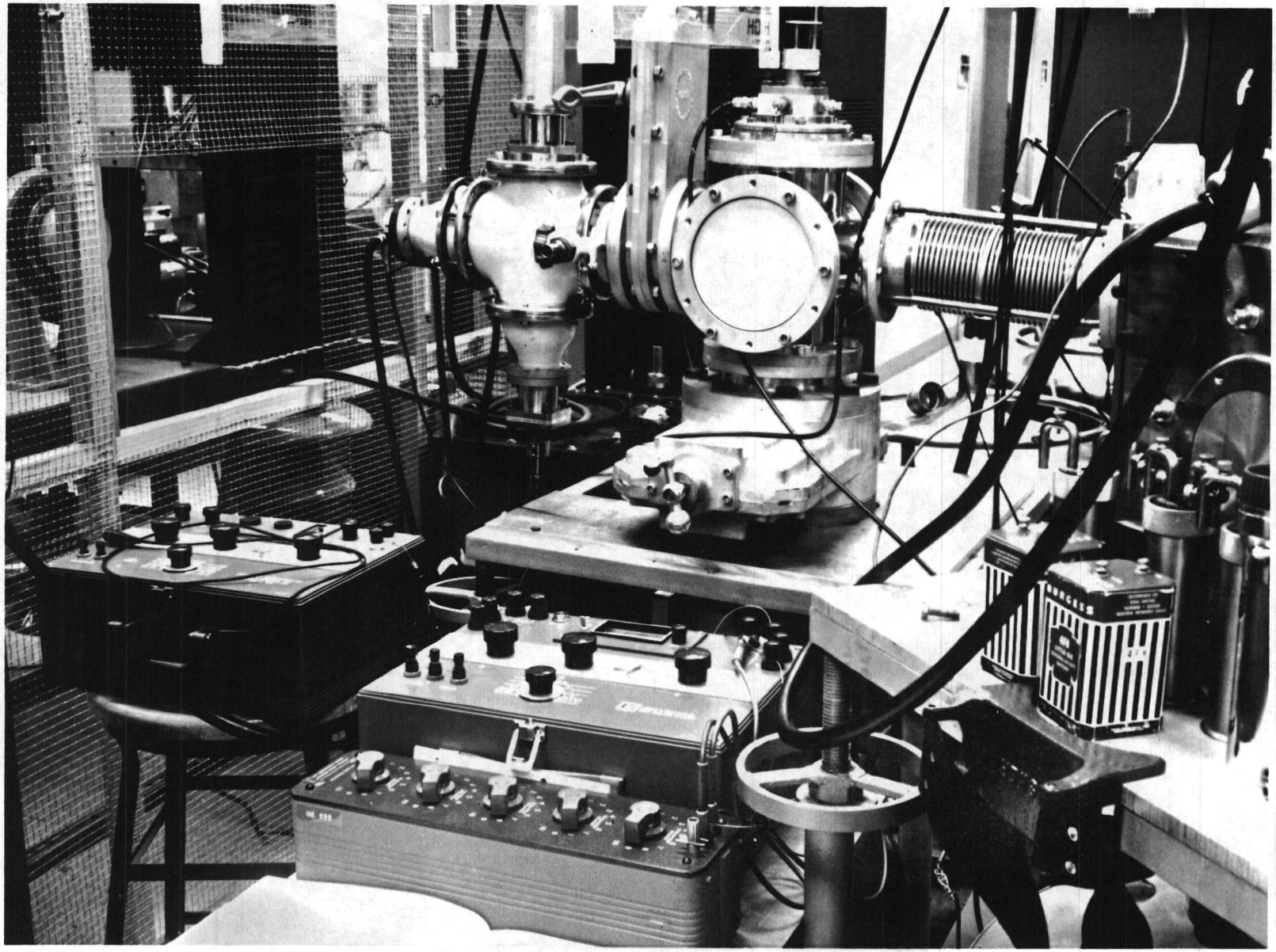

Figure 2. Target region assembly.

a number of sampling points could be gotten over the beam cross-section. A photograph of the wire detector and its mount is shown as Figure 3; the detector assembly inserts into the bottom of the target chamber as sketched in Figure 1. The neutral beam energy flux can be inferred from the measured average change in platinum wire resistance; the neutral beam dose then follows if it is assumed that (1) neutral atom energy is equivalent to that of the ion beam and (2) kinetic energy of neutral atoms is completely absorbed when intercepted by the wire.

2.2 Analysis for Data Reduction

The platinum wire is heated by the beam and, when steady-state is reached, the absolute resistance is measured with an accurate Kelvin Bridge. If the rise in average wire temperature, with respect to its measured end temperature, is limited to a few hundred degrees centigrade, a linear relation holds between average incremental resistance and average incremental wire temperature;

$$\langle T_p \rangle = \frac{\langle r \rangle}{\alpha\, r_{ref}}$$

$$\alpha = .0039\ ^{\circ}C^{-1} \qquad (1)$$

(r_{ref} is resistance of wire prior to beam heating)

where platinum properties are taken from a monograph by Caldwell. Note that an accuracy for $\langle T_p \rangle$ determination of $\sim$ 2.5% is implied. Figure 4 outlines the experimental technique for determining $\langle T_p \rangle$ from which beam power density can be inferred for a given position of the wire in the beam.

A steady-state heat balance is performed, and an average heat flux can be calculated for a given $\langle T_p \rangle$. The one-dimensional governing equation is fourth degree, subject to fixed wire end temperature.

$$\pi R^2 k \frac{d^2T}{dx^2} - 2\pi R\varepsilon\sigma(T^4 - TA^4) + 2RH = 0 \qquad (2)$$

Terms have dimensions watts per unit length of wire. Energy loss from the wire is attributed to axial conduction (x - direction) and black-body radiation; k is thermal conductivity, ε emissivity, σ Stephan-Boltzman constant, TA enclosure temperature, and other symbols are made clear in Figure 4. Boundary conditions are,

$$\frac{dT}{dx}(0) = 0$$

$$T(L) = TEND \qquad (3)$$

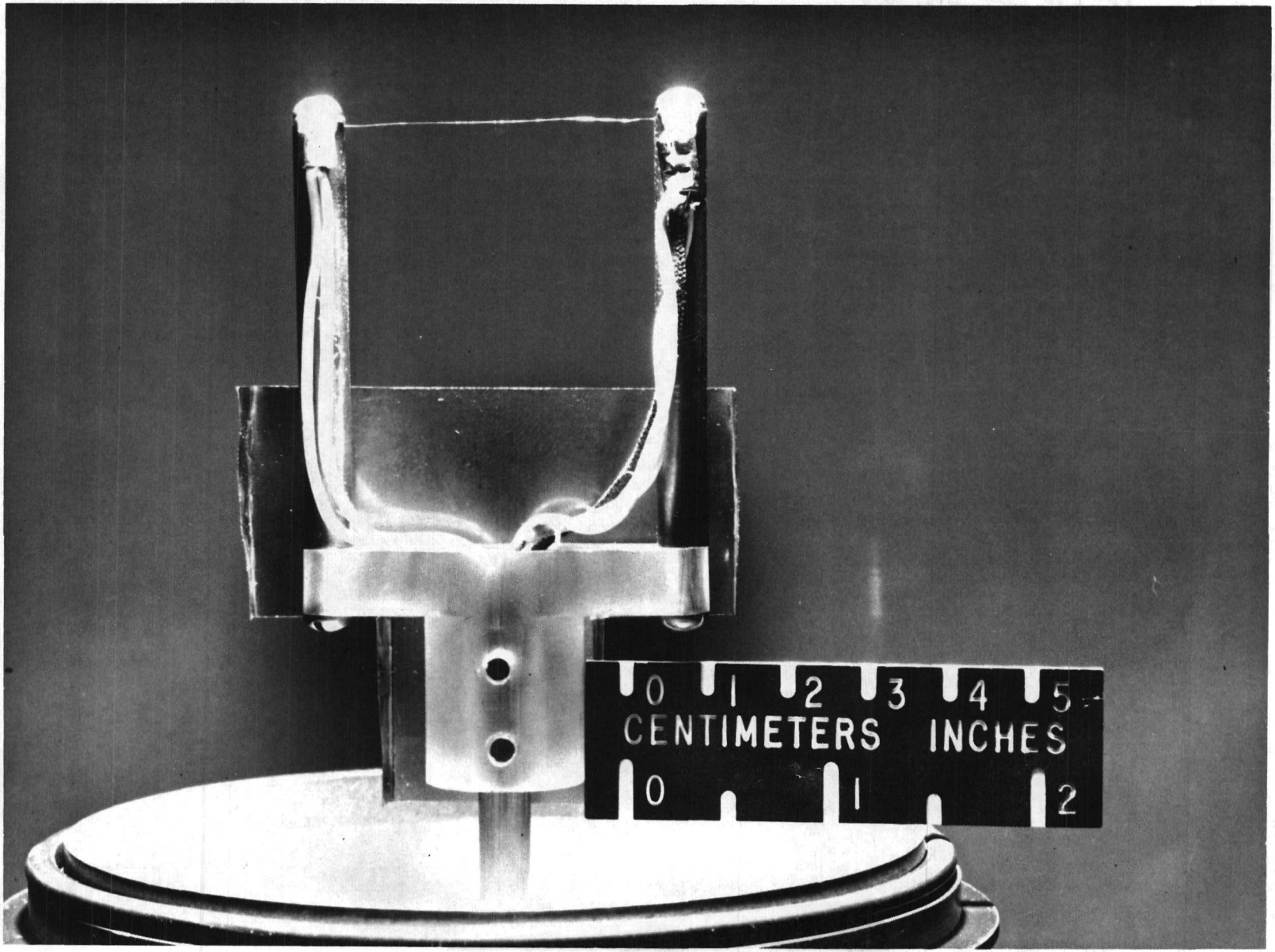

Figure 3. Wire detector assembly.

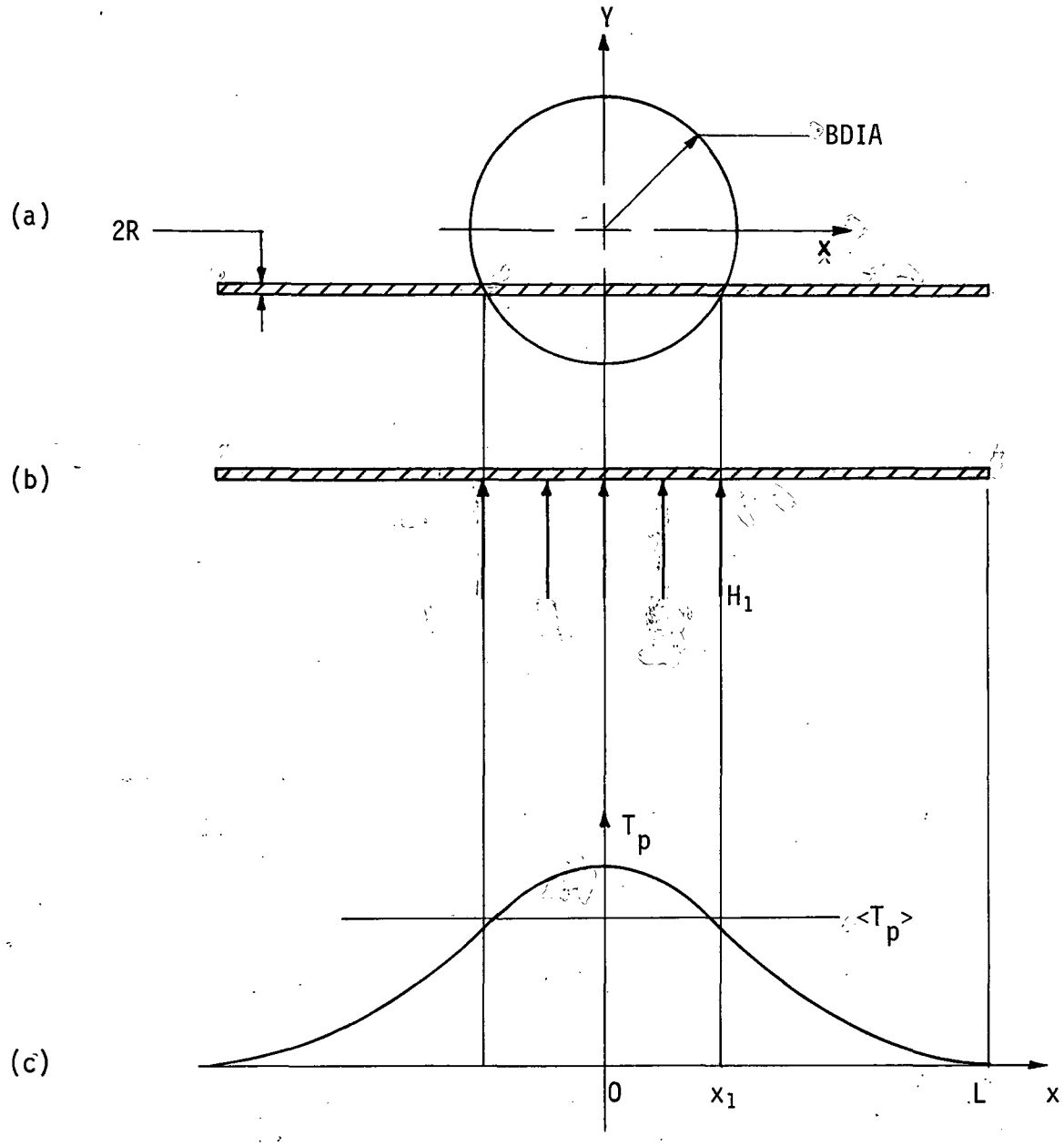

Figure 4. Method of determining beam power density.

(a) Platinum wire subtends cord in beam of diameter BDIA >> 2R, (b) energy of beam, H_1(watts/cm^2) is absorbed until losses balance gains, (c) a steady state temperature profile obtains with $\langle T_p \rangle$ the experimentally determined average incremental temperature, x_1, the half-heated length, and L, the half-wire length.

The problem of data reduction amounts to the determination of the power density of an incident beam given:

(1) the average temperature of the wire
(2) the position of the wire in the beam
(3) the beam diameter
(4) the rod end temperature, TEND
(5) the ambient (enclosure) temperature, TA

A great deal of information is revealed by studying the solution to the linearized equation.

Define

$$T(x) = TA(T_p(x)/TA + 1) \tag{4}$$

where $T_p(x)/TA$ is small compared with unity. By performing the Taylor Series expansion of $(T(x)^4 - TA^4)$, replacing $T(x)$ with the previous definition and applying the perturbation condition a new differential equation in $T_p(x)$ results,

$$\frac{d^2}{dx^2} T_p(x) - \frac{8\varepsilon\sigma(TA^3)}{Rk} T_p(x) + \frac{2\ H(x)}{k\pi R} = 0 \tag{5}$$

where,

$$H(x) = H_1, \text{ constant } 0 \leq x \leq x_1$$

$$0, \ x_1 < x < L$$

The new boundary conditions are,

$$0 < x < x_1 \begin{cases} \dfrac{dT_p(0)}{dx} = 0 \\ \dfrac{dT_p(x_1^-)}{dx} = \dfrac{dT_p(x_1^+)}{dx} \end{cases} \tag{6}$$

$$x_1 < x \leq L \begin{cases} T_p(x_1^-) = T_p(x_1^+) \\ T_p(L) = TEND - TA \end{cases} \tag{7}$$

Solutions can be obtained as follows:

For $0 \leq x \leq x_1$

$$T_p(x) = (Q_1/B_1) + C_2 \cosh(\sqrt{B_1}\ x) \tag{8}$$

For $x_1 < x \leq L$

$$T_p(x) = F_1 \sinh(\sqrt{B_1}(L-x)) + (TEND - TA) \cdot \cosh(\sqrt{B_1}(L - x)) \tag{9}$$

The incremental temperature distribution is algebraic in $Q_1(\propto H_1)$. The average incremental temperature for a particular H_1 value is obtained by integrating equations (8) and (9);

$$\langle T_p \rangle = \frac{1}{L} \int_0^L T_p(x)\, dx$$

$$= \frac{1}{L} \left[\int_0^{x_1} T_p(x)\, dx + \int_{x_1}^{L} T_p(x)\, dx \right] \tag{10}$$

$$\langle T_p \rangle = \frac{1}{L} \left\{ (Q_1/B_1)\, x_1 + \frac{\hat{C}_2}{\sqrt{B_1}} \sinh(\sqrt{B_1} x_1) \right.$$

$$+ \frac{F_1}{\sqrt{B_1}} \left[\cosh(\sqrt{B_1}(L - x_1)) - 1 \right] \tag{11}$$

$$\left. + \frac{(TEND - TA)}{\sqrt{B_1}} \sinh(\sqrt{B_1}(L - x_1)) \right\}$$

Equation (11) can be inverted to solve for Q_1 in terms of the measured value $\langle T_p \rangle$. Defining,

$$QBAR = x_1 Q_1 k \pi R = 2x_1 H_1 \tag{12}$$

which is the heating rate per unit wire diameter, the following working expression results:

$$QBAR = A_1 \langle T_p \rangle - A_2(TEND - TA) \tag{13}$$

The constants, B_1, Q_1, C_2, A_1 and A_2 are written out in the Appendix. Thus QBAR is determined algebraically from the experimental and physical data.

In the event that $T_p(x)/TA$ is <u>not</u> small compared with unity, the non-linear equation must be solved. A computer program has been written to calculate the beam power per unit wire diameter, QBAR, corresponding to a given average incremental temperature. This is accomplished by assuming an upper bound on QBAR and iteratively converging to the actual QBAR which corresponds to the

given average incremental temperature. Comparison of results from the closed form solution and the iterative method showed good agreement when a linear case was tested.

2.3 Results

The incremental change in resistance of the platinum wire was determined for various y-positions in the beam (see Figure 4), with set values of target region pressure, beam energy and ion current at the beam stop. Via equation (1) these values were converted to average incremental temperature rise. Typical curves of $\langle T_p \rangle$ versus arbitrary y-position are presented in Figure 5. The beam boundaries are well defined; however, the beam power density distribution in the vertical direction through the beam is skewed upward; such was true in most but not all beam profiles. This behavior relates closely to beam forming and focusing properties determined outside the target region of the system. A non-zero "smear" condition is detected at the top edge of the neutral beam, which is attributed to straggling ions and neutral atoms. These particles are diverted from the principal direction of neutral beam flow at the position where vertical deflection plates send the ion beam along the tube above the neutral beam to the ion beam stop. Since the neutral beam edges were generally distinct and the neutral particle content in the "smear" region was clearly small, extrapolation to establish beam diameter, BDIA, was performed on the curves on Figure 5. Note that the data points were joined with a smooth curve, and a circular beam cross section was assumed, consistent with the mechanism of electrostatic ion beam focusing. Besides beam diameter, information regarding temperatures TA and TEND was needed before employing the data reduction scheme outlined in section 2.2. The wire end temperature was taken to be that of the massive stainless steel mounts shown in Figure 3 to which was attached an iron-constantan thermocouple junction. The enclosure temperature, TA, was taken as that of the ambient atmosphere in contact with the target chamber outer surface.

Calculations were consequently made to determine QBAR versus y, the vertical position of the detector wire in the beam. The curves of Figure 5 are consequently reduced to those shown in Figure 6. Recalling that QBAR is the heat rate per unit wire diameter, it is clear that the total neutral beam power is determined by integration after connecting the data points using a smooth curve; integration of the asymmetric beam profiles was performed mechanically. Neutral beam powers for the cases shown in Figure 6 are,

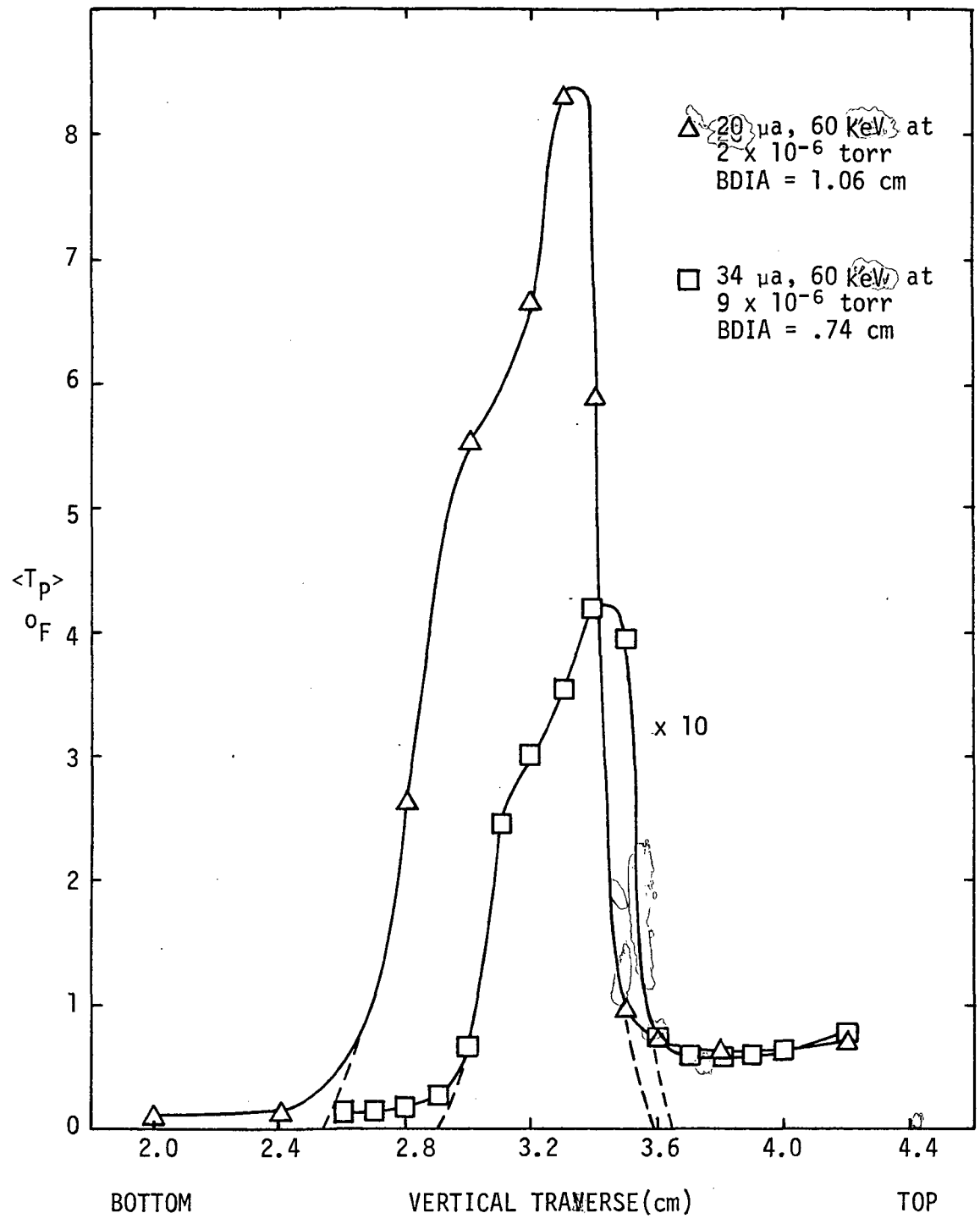

Figure 5. Typical <T_p> data for neutral beams.

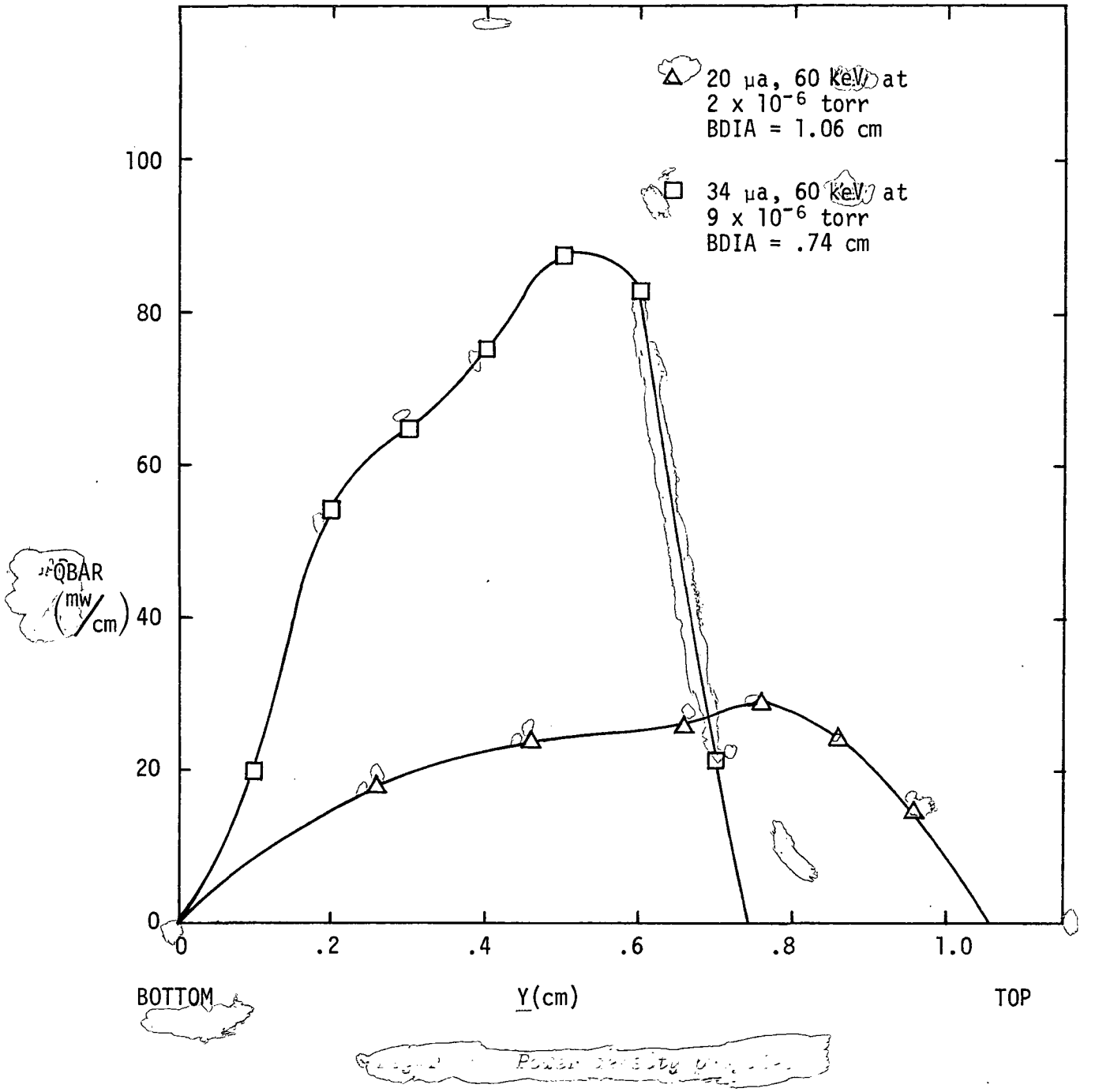

Figure 6. Power density profiles.

□ 40.4 milliwatts

△ 20.3 milliwats

compared with ion beam powers of 34 μa x 60 kV = 2.04 watts, 20 μa x 60 kV = 1.20 watts respectively. The ion beam currents were estimated from measurements made with a Faraday cup shielded against secondary electron loss.

2.3.1 Pressure Effect. Two cases were performed under the following conditions:

	Pressure(torr)	
	2×10^{-6}	9×10^{-6}
Ion current (μa)	34	34
beam potential (kV)	60	60
TEND (°R)	524.7	530.2
TA (°R)	533.7	534.7
BDIA (cm)	1.15	.74
neutral beam power (mw)	13.5	40.4

The 9×10^{-6} torr case is displayed as the □-data in Figures 55 and 66. The higher pressure data would be expected to yield a greater neutral beam power in direct ratio to the pressures, *i.e.*, 4.5 to 1.0. The neutral beam power ratio found is in ratio 3.0 to 1.0. This discrepancy is due mainly to the inequality in TEND values (a difference of 5.5°R) resulting in a higher neutral beam power for the low pressure case. It is not clear why the reference temperature of the wire mount, which did not vary widely while data was taken, should be lower in the low pressure case. The BDIA difference is due to focusing irregularities, but this should have no effect on neutral beam production so long as the ion currents are equal and the beam diameters remain large compared with mean spacing between background gas atoms.

2.3.2 Self-Consistency Test. The wire detector was scanned through both the neutral beam and the total beam (neutrals plus ions) in a sequence of experiments. A separate measurement of the ion beam current was made with the shielded Faraday cup. A power balance was attempted such that,

$$\dot{Q}_{n+i} = \beta \dot{Q}_n + \dot{Q}_i \qquad (14)$$

The symbols represent heating rate due to total beam, neutral beam, and the ion beam respectively. The factor $\beta (= 2.63)$ is a geometric factor gauging that length of the beam tube over which fast neutrals were produced by charge transfer. For a 40μa, 60 keV ion beam at 2×10^{-6} torr the results are,

$$.981 \overset{?}{=} (2.63)\,(.018) + 2.400 \text{ [watts]}$$

$$\neq 2.447$$

The discrepancy is attributed to (1) secondary electron emission problems in measuring ion beam current and (2) secondary processes occurring at wire surface while scanning the total beam. Ion scattering, secondary emission and sputtering processes on the platinum wire would cause a portion of the total beam energy not to be deposited, hence the measured value, $\dot{Q}_{n+i} = .981$ watts, would be less than actual total beam power. It is difficult to believe that surface processes alone could account for the factor of 2.5 difference in deposited power. Both types of errors must share the discrepancy. It is possible that there is a spread in ion beam energy, although small for a magnetically analyzed beam, such that every ion does not carry 60 keV kinetic energy as has been assumed in calculating $\dot{Q}_i$. In considering the fraction of ion beam which is neutralized, the ratio is .018 watts/2.400 watts $\approx$ .8%, a value not inconsistent with the 1% reported by McGinty, *et al.*, using a 34μa, 60 keV phosphorus beam with BDIA = .8cm.

3. SPUTTERING MECHANICS

A vast literature exists describing ingenious experiments elucidating sputtering phenomena induced by primary ions ranging in energy from threshold values of a few tens of eV to the meV region (see summaries by Kaminsky, and Carter and Colligon). No significant progress was made in this present study with respect to quantitative details of argon ion or dopant ion sputtering on semiconductors.

3.1 Semiconductor Sputtering

A few papers were found (published between 1967 and 1971) mainly addressing the question of compositional carry-over to substrate and experimental sputtering yield comparisons with various theories. A paper by Comas and Cooper reports experiments where single crystal GaAs was sputtered by normally incident low energy argon ions; composition of sputtered material and yield values are offered as results. In section 7.9 of the work by Carter and Colligon it is reported that the composition of sputtered material from GaSb and InSb samples is basically stoichiometric. In the paper by Sommerfeldt, *et al.*, 30 keV argon ions bombarded a single crystal of germanium. By controlling target temperature they were able to study sputter yield and secondary electron emission for ordered and amorphous states of the same target. The theory of

focused collision events along close-packed atomic rows (focuson mechanism) did not explain their experimental findings. Another paper taking issue with the focuson mechanism was published by Cowell and Smith. Two other papers, relating to semiconductor sputtering, by Hanak also Efremenkova, *et al.*, are listed in the reference section.

Two conclusions can be drawn from these few recent works: (1) sputter theory and experiment have not yet been brought into good agreement (Kaminsky, Carter and Colligon, Sommerfeldt, *et al.*, Cowell and Smith), and (2) composition of certain semiconductor materials carries over essentially in stoichiometric ratio (Carter and Colligon, Comas and Cooper).

3.2 Isotropic Sputtering Model

If it is assumed that sputtered molecules have no preferred direction of departure, as is often the case for polycrystalline materials, the directional concentration of sputtered molecules would follow the cosine law:

$$S_n = A \cos \theta \tag{15}$$

where S_n is the number of molecules leaving in the direction θ, A is a constant and θ is the angle between the surface normal and the molecular path. Aside from a difference in velocities, this type of scattering is exactly analogous to gray diffuse radiation theory. As a result, the sputtered yield between two finite areas can be determined using radiation enclosure theory.

According to Hamilton and Morgan, the fraction of molecules leaving a differential area dA_1 and arriving at an arbitrarily inclined rectangular area A_2 (see Figure 7) would be

$$F_{dA_1 \to A_2} = \frac{1}{2\pi(dA_1)} \left\{ \tan^{-1} M + \left(\frac{H \cos \phi - 1}{\sqrt{1 + H^2 - 2H \cos \phi}} \right) \tan^{-1} \cdot \left(\frac{M}{\sqrt{1 + H^2 - 2H \cos \phi}} \right) + \frac{M \cos \phi}{\sqrt{M^2 + \sin^2 \phi}} \left[\tan^{-1} \left(\frac{H - \cos \phi}{\sqrt{M^2 + \sin^2 \phi}} \right) + \tan^{-1} \left(\frac{\cos \phi}{\sqrt{M^2 + \sin^2 \phi}} \right) \right] \right\} \tag{16}$$

where $M = {}^{m}/_{a}$ and $H = {}^{h}/_{a}$, (m, n and a are shown in Figure 7). Conversely, the number of molecules leaving area A_2 and arriving at dA_1 would be:

$$n A_2 F_{A_2 \to dA_1}$$

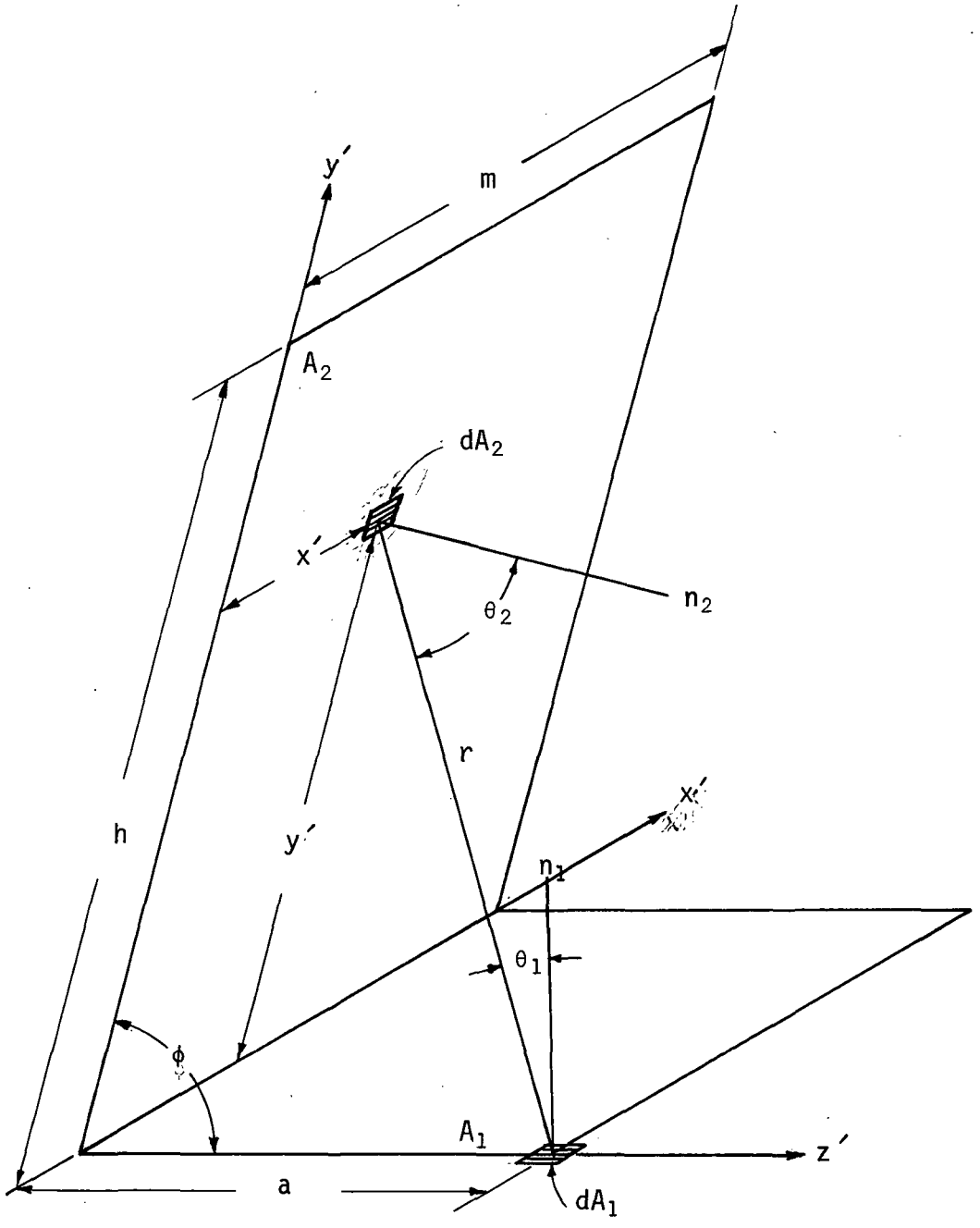

Figure 7. Target-substrate geometry.

where n is the number flux leaving A_2 (molecules per square cm per second). From radiation theory,

$$F_{A_2 \rightarrow dA_1} = \frac{dA_1}{A_2} F_{dA_1 \rightarrow A_2} \tag{17}$$

Hence,

$$nA_2 F_{A_2 \rightarrow dA_1}$$

$$= \frac{n}{2\pi}\left[\tan^{-1} M + \frac{H \cos \phi - 1}{\gamma} \tan^{-1} \frac{M}{\gamma} + \frac{M \cos \phi}{\beta} \right. \tag{18}$$

$$\left. + \frac{M \cos \phi}{\beta}\left(\tan^{-1} \frac{H - \cos \phi}{\beta} + \tan^{-1} \frac{\cos \phi}{\beta}\right)\right]$$

where

$$\gamma^2 = (1 + H^2 - 2 H \cos \phi) \text{ and } \beta^2 = M^2 + \sin^2 \phi$$

Consequently, the sputtering yield on a surface can be estimated by calculating $F_{A_2 \rightarrow dA_1}$ for all dA_1 on the receiver surface.

If more than one target material is used simultaneously and each material is a separate rectangular area, the relative concentrations can be determined by breaking the target up into an appropriate number of rectangular areas and analyzing each rectangle separately. Then, the concentration at each dA_1 can be determined for each constituent and the relative concentrations can be determined by dividing the number of molecules of a particular constituent by the total number of molecules.

As a test case a target-substrate system as shown in Figure 8a was studied. Initially, the target was assumed homogeneous and the local yield was determined by dividing the substrate (receiver) surface into 0.25 x 0.25 cm differential areas, then calculating $F_{A_2 \rightarrow dA_1}$ to the center of each "differential" area. The relative yields across the substrate surface are shown in Figure 8b, where S/S_{target} is the fraction of sputtered material arriving at the substrate.

As a second case, it was assumed that the target was divided into two equal areas -- a left half and a right half -- of dimension $\frac{T_L}{2} \times T_W$. It was assumed that the target materials A and B each had the same yield under ion bombardment, hence the flux expressions (17) and (18) are valid. Naturally, the same total concentration was computed as before. The relative

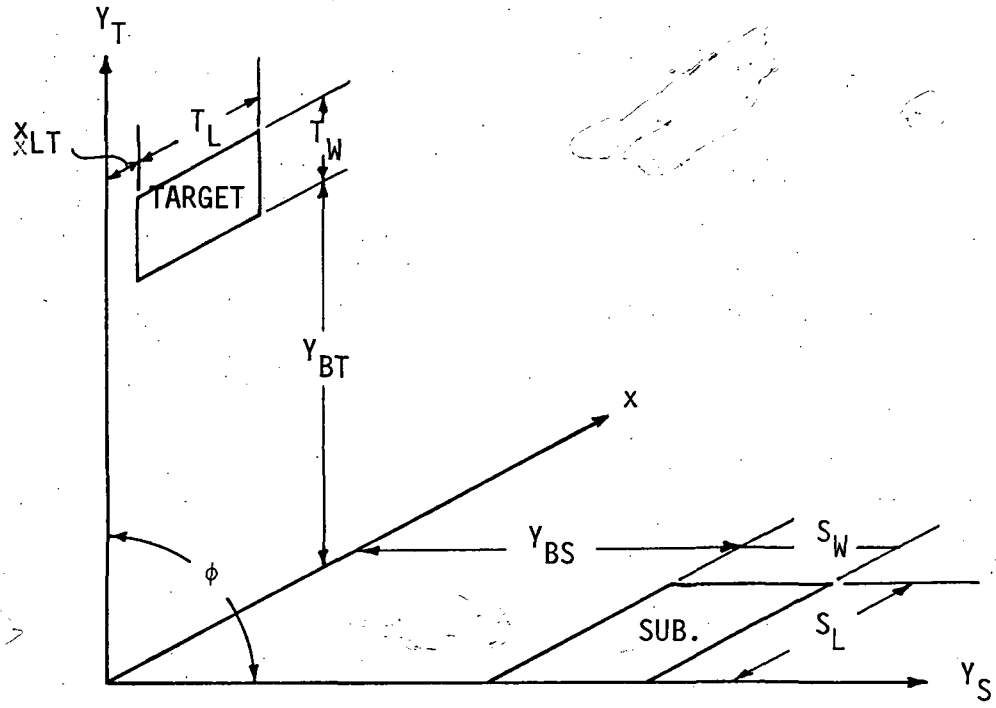

Figure 8a. Computed density distributions on the substrate (geometry.)

$x_{LT} = 0.5$, $T_L = 2$, $T_W = 1$, $Y_{BT} = 5$, $Y_{BS} = 5$, $S_W = 2$, $S_L = 3$, $\phi = 90°$

(All dimensions in centimeters)

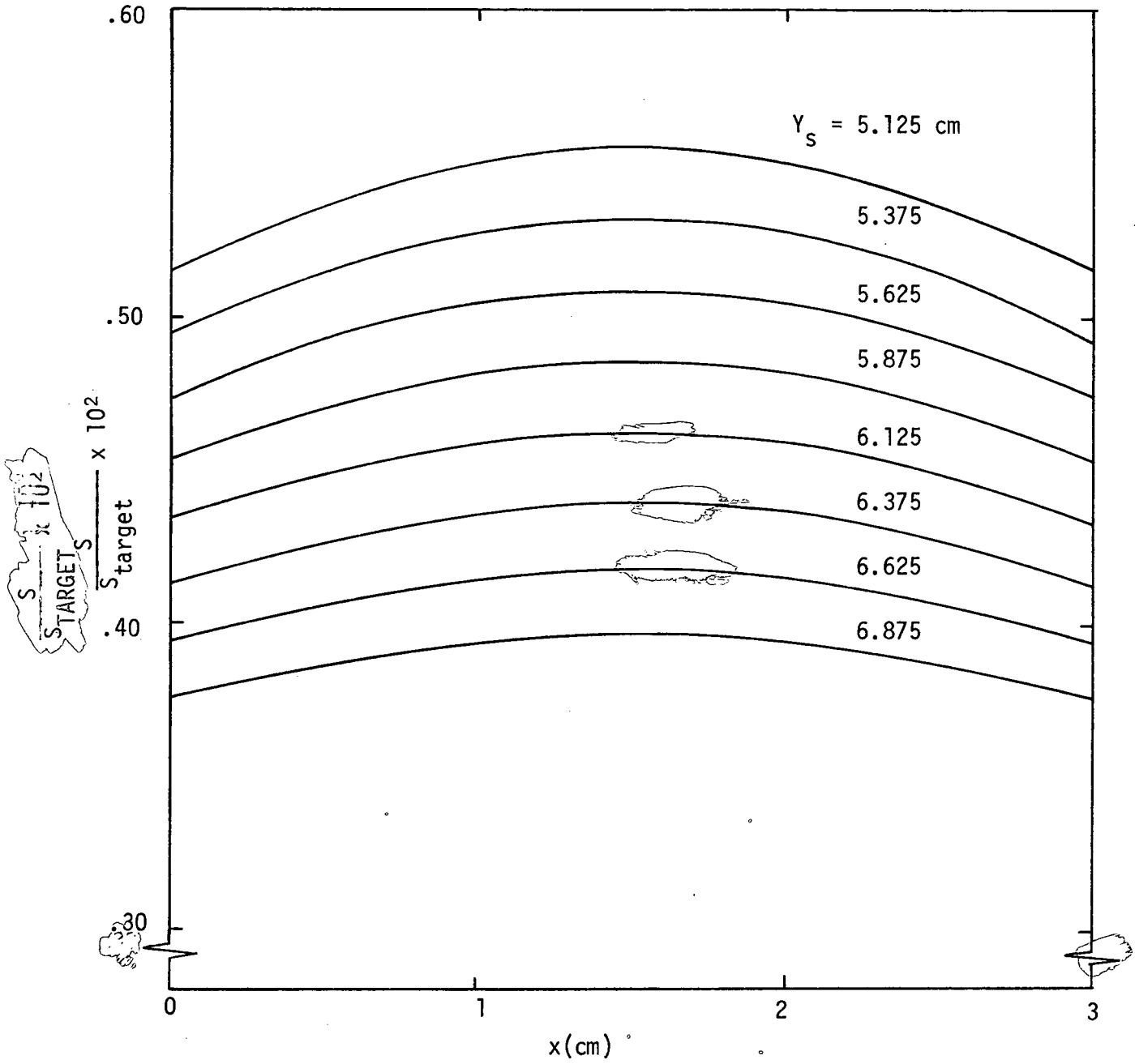

Figure 8b. Computed density distributions on the substrate.

x_{LT} = 0.5, T_L = 2, T_W = 1, Y_{BT} = 5, Y_{BS} = 5, S_W = 2, S_L = 3, ϕ = 90°

(All dimensions in centimeters)

concentration of A -- the left material -- on the substrate was calculated via a computer program. Reasonable results were obtained in tabular form. Since no experimental results were available to compare with model calculations, the tabular values are not presented here.

4. CONCLUSIONS

The main contribution of this work was to establish a method of determining neutral beam flux, dose, or power density. An energy deposition technique was used, and chord-wise sampling of beam power density distributions gave some fine structure information. Certain secondary processes at the detector wire surface limit the accuracy of the technique. The "resolution" of the detector was not determined, but neutral beams of approximately 1% ion beam equivalent current were detected and beam profiles measured. Integration of beam profiles yielded total neutral beam power.

The method could be further studied in order to establish the accuracy of the technique. For the instrument to be used as an on-line monitoring device, an automatic scanning and resistance read-out system could be devised. As conceived the instrument serves mainly as a research tool.

A model successfully representing sputter material transport from target to substrate was constructed. Some analytic results are presented, but no experimental data was found to compare with model calculations.

5. ACKNOWLEDGEMENTS

Expert laboratory work was performed making the neutral beam measurements possible. The authors particularly wish to thank two people in the Instruments Techniques Section of IRD. Tucker Clark contributed to beam detector design, fabrication, and experimental assembly. Johnny Burgess was a patient and talented operator of the complex high-vacuum ion beam system.

6. REFERENCES

Berkner, K.H., Myers, B.R., and Pyle, R.V., "Pyroelectric Ceramics as Detectors of Fast Atomic Beams," Rev. Scien. Instru., 38, no. 8, 1204-06 (August 1968).

Caldwell, F.R., Thermocouple Materials, National Bureau of Standards Monograph 40, March 1, 1962.

Carter, G. and Colligon, J.S., Ion Bombardment of Solids, Heinenann Educational Books, Ltd., London, 1968.

Comas, J. and Cooper, C.B., "Mass-Spectrometric Study of Sputtering of Single Crystals of GaAs by Low-Energy A Ions," J. Appl. Phys., 38, no. 7, 2956-60 (June, 1967).

Cowell, G.K. and Smith, H.P., Jr., "Measurement of Sputtered-Particle Velocity Spectra," J. Appl. Phys., 43, no. 2, 412-16 (February, 1972).

Efremenkova, V.M., *et al.*, "Surface Structure; Sputtering and Scattering of Ions from $A^{II}B^{VI}$ Single Crystals (CdS, CdSe, CdTe)" Proc. 7th Inter. Cong. on Elect. Microscopy, Grenoble, France, 30 Apr. '70 (Paris, France; Soc. Francaise de Microscopic Electronique 1970) pp. 249-50.

Hamilton, D.C. and Morgan, W.R., "Radiation-Interchange Configuration Factors," Excerpts from N.A.C.A. TN 2836.

Hanak, J.J., "Compositional Determination of r.f. co-sputtered Multicomponent Systems," J. Vac. Sci. & Tech., 8, no. 1, 172-5 (Jan.-Feb. 1971) -- Several other articles in this number.

Huddlestone and Leonard, Plasma Diagnostic Techniques, Academic Press, New York, 1965.

Kaminsky, M., Atomic and Ionic Impact Phenomena on Metal Surfaces, Academic Press, New York, 1965.

McGinty, G.K., Goldsmith, B.L., and Thomas, R.A., "A 200Kv Ion Implantation Equipment at M.R.L., Salfords," European Conference on Ion Implantation, Reading, England, September 7-9, 1970.

Ormrod, J.H., "Beam Scanner," Rev. Scien. Instru., 40, no. 9, 1247-48 (September, 1969).

Sommerfeldt, H., Maskova, E.S., and Molchanov, V.A., "On Sputtering of Semiconductors," paper 2.2.1.5, 9th Inter. Conf. on Phenomena in Ionized Gases, Bucharest, Romania, 1969.

APPENDIX

Constants involved in the linear solution of equation (2) for ultimate determination of QBAR are listed here.

$$B_1 = \frac{8\,\varepsilon\,\sigma\,(TA)^3}{Rk}$$

$$Q_1 = \frac{2\,H_1}{k\pi R}$$

$$F_1 = \Big\{(Q_1/B_1) - (TENDA - TA)\,[\sinh(\sqrt{B_1}(L - x_1)) \cdot \frac{\cosh(\sqrt{B_1}x_1)}{\sinh(\sqrt{B_1}x_1)} + \cosh(\sqrt{B_1}(L - x_1))]\Big\}/\{\sinh(\sqrt{B_1}(L - x_1)) + \cosh(\sqrt{B_1}(L - x_1))\cosh(\sqrt{B_1}x_1)/\sinh(\sqrt{B_1}x_1)\}$$

$$C_2 = \{-F_1 \cosh(\sqrt{B_1}(L - x_1)) - (TEND - TA) \cdot \sinh(\sqrt{B_1}(L - x_1))\}/\sinh(\sqrt{B_1}x_1)$$

$$A_1 = (k\,\pi\,R\,L)D_2$$

$$A_2 = k\,\pi\,R\,D_2\left(\frac{1}{\sqrt{B_1}}\right)[\sinh(\sqrt{B_1}(L - x_1) \cdot \frac{\cosh(\sqrt{B_1}x_1)}{\sinh(\sqrt{B_1}x_1)} + \cosh(\sqrt{B_1}(L - x_1))]/D_1$$

$$D_1 = \left\{\sinh(\sqrt{B_1}(L - x_1)) + \cosh(\sqrt{B_1}(L - x_1)) \cdot \frac{\cosh(\sqrt{B_1}x_1)}{\sinh(\sqrt{B_1}x_1)}\right\}$$

$$D_2 = \left\{1/\left[\frac{1}{B_1} - \left(\frac{1}{x_1(B_1)^{3/2}\,D_1}\right)\right]\right\}$$

DISTRIBUTION LIST
NAS1-9434-43

3

	No. Copies
NASA Langley Research Center Hampton, VA 23665	
Attn: Report & Manuscript Control Office, Mail Stop 180A	1
Raymond L. Zavasky, Mail Stop 115	1
James A. Hutchby, Mail Stop 499	1
William E. Miller, Mail Stop 499	1
Joseph S. Heyman, Mail Stop 499	1
Rosa C. Webster, Mail Stop 499	1
Stewart L. Ocheltree, Mail Stop 234	1
Herbert D. Hendricks, Mail Stop 499	10
NASA Ames Research Center Moffett Field, CA 94035	
Attn: Library, Mail Stop 202-3	1
NASA Flight Research Center P. O. Box 273 Edwards, CA 93523	
Attn: Library	1
NASA Goddard Space Flight Center Greenbelt, MD 20771	
Attn: Library	1
NASA Lyndon B. Johnson Space Center 2101 Webster Seabrook Road Houston, TX 77058	
Attn: Library, Code JM6	1
NASA Marshall Space Flight Center Huntsville, AL 35812	
Attn: Library	1
Jet Propulsion Laboratory 4800 Oak Grove Drive Pasadena, CA 91103	
Attn: Library, Mail 111-113	1
NASA Lewis Research Center 21000 Brookpark Road Cleveland, OH 44135	
Attn: Library, Mail Stop 60-3	1
NASA John F. Kennedy Space Center Kennedy Space Center, FL 32899	
Attn: Library, IS-DOC-1L	1

	No. Copies
National Aeronautics & Space Administration Washington, DC 20546 Attn: KSS-10/Library	1
RE/NASA Headquarters	1
NASA Scientific & Technical Information Facility P. O. Box 33 College Park, MD 20740	13 plus reproducible